Experimental and numerical investigation of residual stress effects on fatigue crack growth behaviour of S355 steel weldments

Anais Jacob[a], Ali Mehmanparast[a,*], Riccardo D'Urzo[a], Joe Kelleher[b]

[a] Offshore Renewable Energy Engineering Centre, Cranfield University, Bedfordshire MK43 0AL, UK
[b] Rutherford Appleton Laboratory, ISIS-STFC Facility, Chilton OX11 0QX, UK

ARTICLE INFO

ABSTRACT

Fatigue crack growth tests have been conducted on S355 G10 + M structural steel which is widely used in the fabrication of offshore structures. Fracture mechanics tests have been performed on compact tension specimens with the crack tip located in the heat affected zone. All tests were performed at room temperature in air and the obtained results are compared with the literature data available on a range of offshore structural steels and also the recommended BS7910 trends using the 2-stage law and simplified law. The specimen orientation, with respect to the location of the extraction within the welded plate, has also been examined and discussed in this work. Residual stress measurements have been performed prior to testing by using the neutron diffraction technique. Finally, a numerical model has been developed in order to calculate the effective stress intensity factor range in the presence of residual stresses. The results have shown that the residual stresses play a key role in the fatigue life of the welded structures, especially in the near threshold region.

1. Introduction

With the increase in energy demand, which has resulted in global warming, a challenge for the international community is to reduce greenhouse gas emissions. An efficient source of clean renewable energy, which can help in meeting this target, is offshore wind which can gradually replace a proportion of the Oil and Gas energy supply in the future. Among the different sources of renewable energy, offshore wind has become one of the preferred solutions due to its large-scale deployment potential and significant reductions in its levelised cost in recent years [1–5]. The offshore wind farm installation, operation and in-service condition monitoring all require consideration of a variety of issues. Indeed, due to the offshore turbulence and cyclic loads from wave, wind and current, these offshore structures are subjected to fatigue damage [6]. In order to withstand the critical conditions in harsh environments, the structural integrity of offshore wind turbines needs to be carefully assessed to provide a reliable estimate of the remaining life of these structures.

The great majority of offshore wind turbines are supported using a monopile type of foundation, which has great design advantages as well as minimal footprint on the seabed [7,8]. These support structures are designed to withstand fatigue failure during installation and in-service operation. The manufacturing procedure for offshore wind monopile structures consists of rolling and bending large structural steel plates

and subsequently welding them together in longitudinal and circumferential directions [9]. The design, fabrication and inspection of offshore wind turbine monopile foundations are costly. Therefore, an important challenge is to improve the existing best practice for structural design and integrity assessment of monopiles that are operating in harsh offshore environments with constant exertion of wind and wave loads inducing corrosion-fatigue damage, particularly at the weld regions and in the presence of residual stresses (RS). Materials used in offshore structures are mainly medium to high strength structural steel, chosen due to their corrosion resistance [10]. The studies in the literature have shown that fatigue crack initiation and growth primarily occur at the weld toe, for the as-welded conditions, and at circumferential welds [5]. Depending on the welding procedure, the crack may propagate from the Heat Affected Zone (HAZ) into the Base Metal (BM) in the through thickness direction [5]. More information about the fatigue damage and loading analysis of the monopile foundations can be found in [11,12].

A significant challenge in the offshore wind industry is to provide a reliable assessment of the remaining life of offshore wind turbine monopile support structures, which subsequently impacts on the levelised cost of energy from offshore wind. For this purpose, the influence of residual stresses must be examined to investigate their effect on the fatigue life predictions of offshore wind turbine foundations. In this paper, the fatigue crack growth (FCG) behaviour of S355 structural

Nomenclature		HAZ	Heat Affected Zone
		BM	Base Metal
a	Crack length	RS	Residual stress
a_0	Initial crack length at the beginning of the main fatigue test	UTS	Ultimate Tensile Strength
		SIF	Stress Intensity Factor
a_f	Final crack length at the end of the main fatigue test	C(T)	Compact Tension specimen geometry
α	Normalised crack length	SEN(B)	Single Edge Notched specimen in Bending
ΔK	Stress intensity factor range	PWHT	Post-Weld Heat Treatment
ΔK_{eff}	Effective stress intensity factor range	EDM	Electrical Discharge Machining
$K_{max,RS}$	Stress intensity factor corresponding to P_{max}	FCG	Fatigue Crack Growth
$K_{min,RS}$	Stress intensity factor corresponding to P_{min}	SAW	Submerged Arc Welding
P_{max}	Maximum applied load	GMAW	Gas Metal Arc Welding
P_{min}	Minimum applied load	BC	Boundary Condition
da/dN	Fatigue crack growth rate	FE	Finite Element
f	Frequency	FEA	Finite Element Analysis
B	Specimen thickness	VCCT	Virtual Crack Closure Technique
N	Number of cycles	TOF	Time Of Flight
W	Specimen width	DNV	Det Norske Veritas

steel, which is used in the fabrication of offshore structures, has been examined in air for the HAZ and compared with the data available in the literature. In these comparisons different specimen geometries and thicknesses as well as various welding techniques have been considered. With the focus on S355 structural steel, which is widely used in the fabrication of monopiles, fracture mechanics fatigue crack growth (FCG) tests are carried out on compact tension (C(T)) specimen geometry, with the crack tip located in the HAZ in the presence of residual stresses. The details of the specimen extraction method and the test procedure for FCG testing in air are presented below. Also presented in this paper are the results of residual stress measurements from neutron diffraction as well as a numerical approach for evaluation of the effective Stress Intensity Factor (SIF) range using ABAQUS CAE software.

2. Specimen design and extraction

The material used in this study is EN-10225:09 S355 G10 + M, which is widely used in offshore applications and especially in the manufacture of offshore wind turbine foundations. The multi-pass submerged arc welding (SAW) technique was used to fabricate a double V-grooved welded plate with the thickness of 90 mm. The overall dimensions of the welded plate were 90 mm (in through thickness direction) × 200 mm (in longitudinal direction) × 600 mm (in transverse direction). It is worth noting that in the fabrication of monopiles, the weld toes can be ground flush or remain in the as-welded condition, as described in Det Norske Veritas (DNV) standard recommendations [13]. In this study the welded plate was used in the as-welded condition, with no post-weld heat treatment (PWHT), to replicate common practice in the offshore wind industry. The yield stress, σ_y, and ultimate tensile strength (UTS) of the material used in this study, with more details on the tensile test, can be found in [9].

As schematically shown in Fig. 1, due to lateral wind and wave loads, crack initiation in monopiles may occur at the circumferential welds located at the outer surface and propagate in the through thickness direction. To replicate the circumferential welds in monopiles, the welded plate mock-up in this study was fabricated to better understand the fatigue crack growth in the HAZ and BM. In order to extract fracture mechanics specimens for testing, 16 mm slices were first cut from the welded plate using the Electrical Discharge Machining (EDM) technique. Each of the extracted slices had the dimensions of 90 mm × 16 mm × 600 mm. EDM machining was used to minimise the machining effects at the outer surface and prevent manufacturing effects on the fatigue test results. C(T) specimens with the width of $W = 50$ mm and thickness of $B = 16$ mm were designed according to the ASTM E647 standard test method for the measurement of FCG rates

[14].

Six slices were cut in total to extract six C(T) specimens with the crack tip located in the HAZ, as schematically shown in Fig. 2. In order to identify the exact location of the crack tip, the slices were initially ground, polished and etched to reveal the material microstructure. Grinding of the specimens was achieved using 120, 240 and 1200 wet sandpaper in ascending order mounted on a rotating wheel on a Metaserv grinding machine. Subsequent to grinding and polishing, the surface was etched using 10% Nital solution in order to be able to visualize the three different regions of interest (BM, HAZ and weld metal). Six C(T) specimens, denoted HAZ 1, HAZ 2, HAZ 3, HAZ 4, HAZ 5 and HAZ 6 were extracted from these slices with the crack tip located in the HAZ region (see Fig. 3). The first three specimens (HAZ 1, HAZ 2 and HAZ 3) had the same 180° orientation with respect to the weld geometry. Similarly, the other three samples (HAZ 4, HAZ 5 and HAZ 6) had the same 0° orientation with respect to the weld geometry. All the specimens had the loading axis parallel to the transverse direction with the crack plane oriented along the through thickness direction. As seen in Fig. 3, C(T) specimens were also ground, polished and etched post-manufacture to ensure that the crack tip is located at the pre-identified region within the HAZ and the crack path during fatigue tests is maintained within the HAZ region. It must be noted that no PWHT was
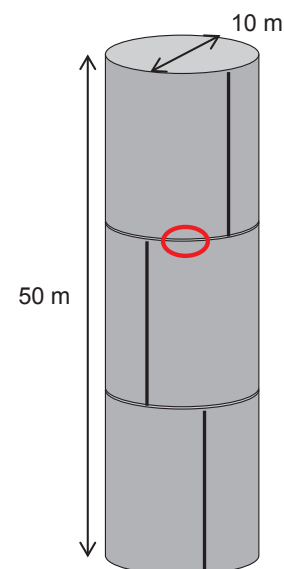

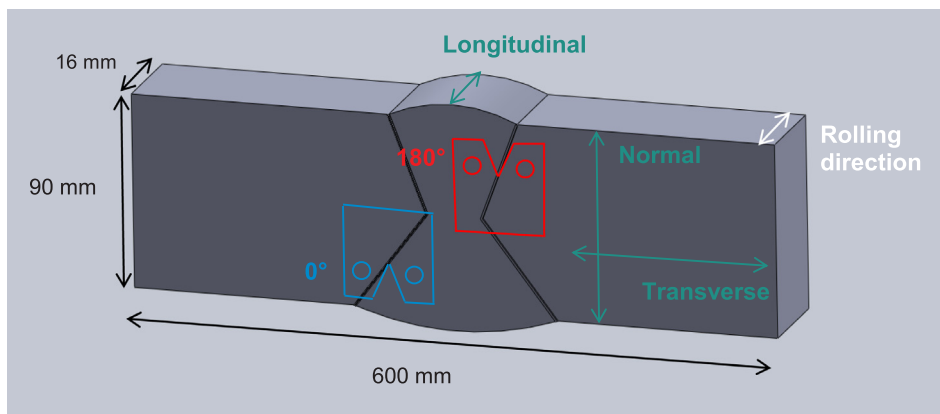**Fig. 1.** Schematic drawing of an offshore wind turbine monopile.

Fig. 2. Schematic representation of a 16 mm thick welded slice and the location of C(T) specimens extracted from the welded slice.
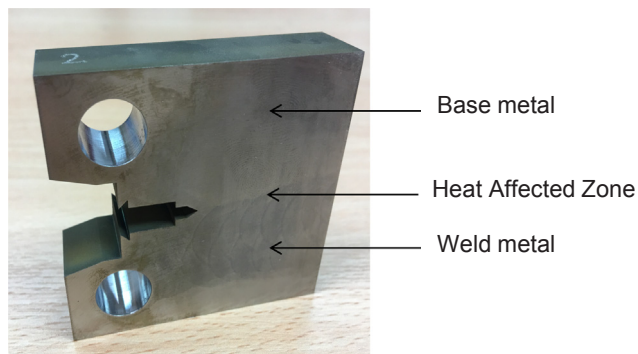

Fig. 3. C(T) sample extracted from the welded plate after polishing and etching.

performed on the extracted slices or C(T) specimens. Although it has been assumed that the level of remaining residual stresses (RSs) in C(T) specimens is relatively low, RS measurements have been conducted on C(T) specimens prior to testing, as described later in this paper, to quantify the level of locked-in RS within the HAZ fracture mechanics specimens.

3. Fatigue crack growth test procedure

FCG tests were performed under Mode I fracture mechanics loading conditions on a standard 100 kN servo-hydraulic fatigue testing Instron machine. The recommendations in the ASTM E647 standard were followed during the test set-up, main phase of fatigue testing and data analysis [14]. All the tests were performed in air with the load ratio of

$R = 0.1$. The tests were conducted at room temperature under load control mode, and both the load and position limits were set in order to ensure that the sample was not overloaded, hence avoiding unexpected plasticity at the crack tip. Sinusoidal cyclic wave form using constant amplitude loading with the frequency of 5 Hz was used for fatigue testing on all three C(T) specimens. Previous studies have shown that, in an air environment, the frequency has negligible effects on the FCG behaviour of steel materials [5].

The initial crack length in C(T) samples, which is reported as the distance between the centre of the pin hole and the machined V-notch in the samples, was 17 mm. All six samples were initially pre-fatigue cracked by approximately 4 mm from the initial V-notch tip using the K-decreasing procedure as suggested in [15]. Particular attention has been given during this process to ensure that the K_{max} value at the end of the pre-cracking stage did not exceed the initial K_{max} value at the beginning of the main FCG test. The crack length was measured, every 5000 cycles, using two cameras positioned in front of both sides of the sample. Individual measurements were conducted on each side and the average value was used as the effective crack length, a. It is worth noting that following instructions provided in ASTM E647, it was ensured that the difference between the crack lengths at the outer surfaces never exceeded 1 mm at any stage of testing, including pre-cracking and the main fatigue testing phase. The experimental set-up, as well as an example of optical crack growth monitoring on C(T) specimens, is presented in Fig. 4.

After pre-fatigue cracking, the main FCG testing was conducted on C(T) specimens and the load levels are summarised in Table 1.

As seen in this table, the maximum and minimum applied loads in all six tests were $P_{max} = 10$ kN and $P_{min} = 1$ kN respectively. The
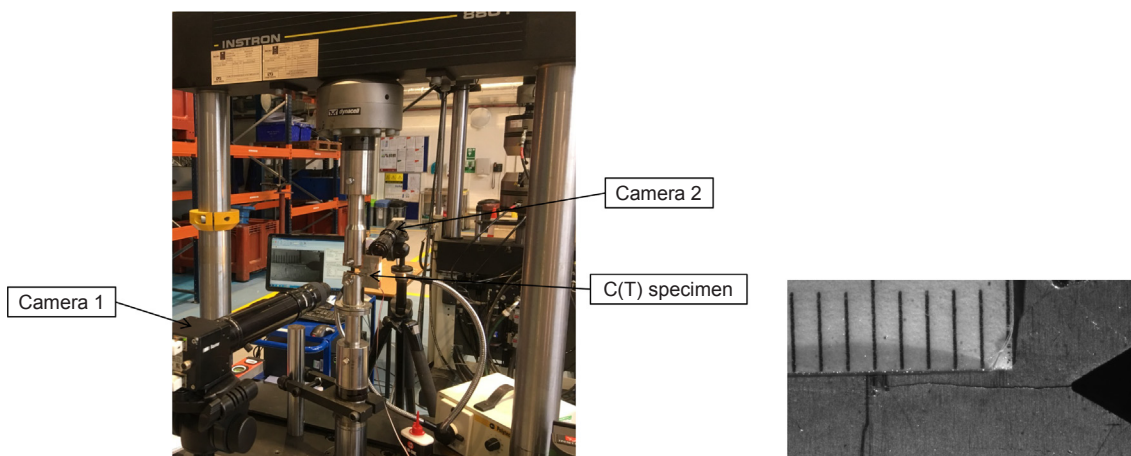

Fig. 4. (a) Fatigue crack growth test set-up, (b) Crack growth monitoring on a C(T) specimen.

Table 1
C(T) specimen dimensions and loading conditions.

	HAZ 1	HAZ 2	HAZ 3	HAZ 4	HAZ 5	HAZ 6
a_0 (mm)	21.2	21.0	21.0	21.0	20.9	20.9
a_f (mm)	35.1	34.6	35.6	35.2	35.0	35.9
W (mm)	50	50	50	50	50	50
B (mm)	16	16	16	16	16	16
P_{max} (kN)	10	10	10	10	10	10
P_{min} (kN)	1	1	1	1	1	1
f (Hz)	5	5	5	5	5	5

instantaneous crack length and fatigue cycle number were captured during the fatigue tests. The FCG rate, *da/dN*, was calculated using a combination of the seven-point incremental polynomial method for most of the obtained data points and the secant method for the first and last three points where enough data points were not available to use the incremental polynomial technique. The SIF range, ΔK, which is suggested for C(T) specimen geometry in ASTM E647, is presented in Eq. (1) [14]. Note that due to the validity limitation of Eq. (1), a new shape function solution for C(T) specimen geometry presented in [5] and shown in Eq. (2) is used to analyse the obtained test data from this study. Note also that as discussed in [5], the ΔK values calculated using Eq. (2) are more accurate for a wider range of normalised crack lengths; $0.2 \leq a/W \leq 0.7$ was used to analyse the data obtained from this study.

$$\Delta K = \frac{\Delta P}{B\sqrt{W}} \times \frac{(2+\alpha)}{(1-\alpha)^{\frac{3}{2}}} \times (0.886 + 4.64\alpha - 13.32\alpha^2 + 14.72\alpha^3 - 5.6\alpha^4) \tag{1}$$

where ΔK is the SIF range, ΔP is the applied cyclic load range, *B* is the specimen thickness, *W* is the specimen width and α is the normalised crack growth length *a/W*.

$$\begin{aligned} Y &= (-372.12\alpha^6 + 1628.60\alpha^5 - 2107.46\alpha^4 + 1304.65\alpha^3 - 391.20 \\ &\quad \alpha^2 + 54.81\alpha + 7.57) \end{aligned} \tag{2}$$

where *Y* is the shape function solution for C(T) specimens and α is the normalised crack length.

4. Fatigue crack growth results

4.1. Analysis of the fatigue crack growth behaviour in the HAZ region

The FCG rate, *da/dN*, for each of the tests conducted in the HAZ specimens is correlated with the SIF range, ΔK, and the results are presented in Fig. 5. The analysis focuses on the Paris region of the FCG curves. As explained in [16,17], the welding residual stresses redistribute in a fracture mechanics test and finally vanish as the crack propagates; however, residual stress effects and the subsequent redistribution have not been considered in the experimental data analysis presented in Fig. 5. As seen in Fig. 5, the FCG trends from all the first three tests on HAZ 1, HAZ 2 and HAZ 3 180° specimens fall on top of each other over the entire ΔK experimental range, indicating a good repeatability across the tests. However, the results from the last three HAZs extracted from 0° orientation display a more sparse distribution. Also included in this figure are the lines of best fit made with the experimental data on the HAZ specimens from 180° and the HAZs from 0° orientation, within the Paris region, to identify the power law constants. The Paris law constants obtained from this fit for the 180° orientation are $C = 1.85 \times 10^{-15}$, $m = 5.10$ with $R^2 = 0.97$ and $C = 1.58 \times 10^{-13}$, $m = 3.96$ with $R^2 = 0.71$ for the 0° orientation. The high value of R^2 from the 180° specimens implies that the line of best fit describes the experimental data trend accurately and that little variation is observed in the FCG behaviour of the HAZ 1, HAZ 2 and HAZ 3 specimens. On the other hand, the lower value of R^2 from the 0° samples suggests a less accurate fit due to the fact that the results are more scattered than the 180° specimens. It can be seen in Fig. 5 that for a given value of ΔK the FCG rate is, on average, around twice higher in specimens with 0° orientation compared to 180° orientation specimens. This difference between FCG behaviour at different specimen orientations might be associated with the change in material microstructure and also the residual stress profile from one crack plane orientation to another.

4.2. Comparison with the literature data

The FCG data on S355 G10 + M structural steel from the HAZ C(T) specimens in this study are compared with the fatigue test data in air available in the literature on other grades of steel that are used in offshore structures as well as the proposed trends in BS7910 standard [18]. More information about the materials used in this section for comparison purposes can be found in Table 2 where the welding
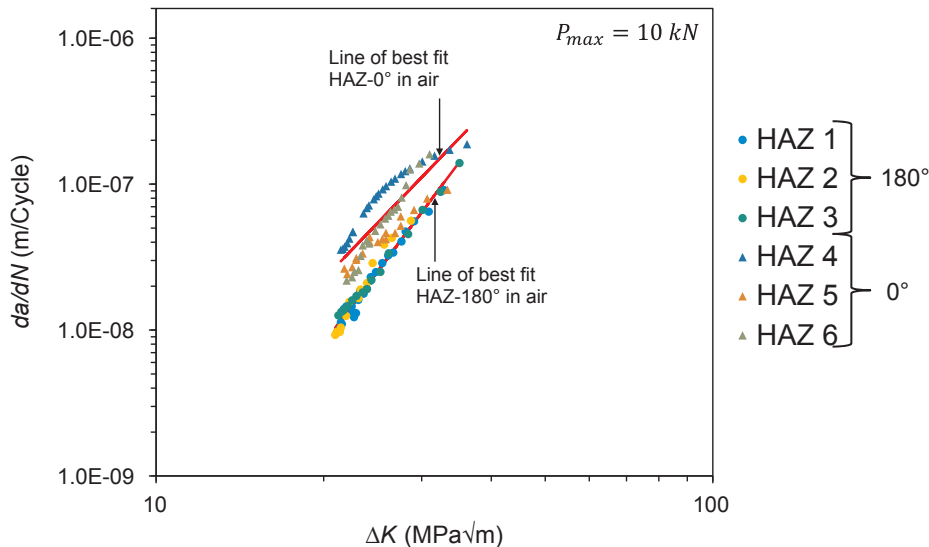

Fig. 5. Fatigue crack growth behaviour of the six HAZ tested samples in an air environment.

Table 2
Specimen specifications and welding process for each HAZ material presented.

	σ_y (MPa)	UTS (MPa)	Specimen geometry	Specimen thickness (mm)	Welding process
S355 G10 + M	455	544	C(T)	16	SAW tandem twin, multi-pass double V-groove hot rolled
S355 G8 + M [5]	413	503	C(T)	16	Multi pass butt-weld double V-groove
S355 NL [21]	345	550	C(T)	32	Butt weld double V-groove
420 MPa structural steel [22]	450	549	SEN(B)	50	SAW
4140 vacuum-degassed high tensile steel [23]	338	577	C(T)	8	SAW U-groove
S355 J2 + N steel [24]	363	535	C(T)	16	WA-Twin/Tandem-twin
S355 EMZ high strength [25]	355	540	C(T)	15	SAW T-joint
SE702 steel [26]	780	850	C(T)	16	SAW K-welded joint
	For 160 mm thick	For 160 mm thick			
C-Mn structural steel [27]	490	510	C(T)	12	GMAW with PWHT
C-Mn-V steel [28]	360	524	C(T)	25	SAW
50D steel [29]	386	536	SEN(B)	15	Single V-groove

processes of the plates and the specimen geometries and thicknesses are summarised. As seen in Table 2 the data collated from the literature are on different ranges of medium to high strength structural steels tested on different specimen geometries with different load levels and specimen thicknesses. The specimen thickness effects on the FCG rate of metallic structures have been investigated in [19,20] and it has been shown that the FCG rate increases by increasing the specimen thickness, due to the higher constraint level in thicker specimens. It must also be noted that the BS7910 curves presented in this study for comparison purposes are based on the mean curves proposed in BS7910 for welded joints in air [18].

All the HAZ materials presented in this section are summarised in Table 2 with the S355 G10 + M structural steel corresponding to the material employed in the current study. The HAZ materials used for comparison are S355 G8 + M [5], S355 NL [21], 420 MPa structural steel [22], 4140 vacuum-degassed high tensile steel [23], S355 J2 + N steel [24], S355 EMZ high strength [25], SE702 steel [26], C-Mn structural steel [27], C-Mn-V steel [28] and 50D steel [29]. Also included in this table are the BM yield stress σ_y and UTS. As seen in Table 2, the majority of the HAZ test data from the literature were gathered from C(T) specimens, whereas Single Edge Notched specimen in Bending, SEN(B), was employed in two of the previous studies. Also seen in this table is that the specimen thickness ranges from 8 mm to

50 mm for various materials used for comparison in this study. The FCG rate data from the present study on HAZ material are plotted against the SIF range and compared with the literature data and BS7910 curves in Fig. 6. As seen in this figure, the majority of the FCG curves obtained from the tests on different steels fall close to each other with the test results presented by Bertini [27] and Albuquerque et al. [21] on C-Mn structural and S355 NL steels, respectively, falling significantly below the main population of fatigue data on other steels. This might be associated with relatively low load levels, in association with the given specimen thickness, employed in these two studies. Also the fact that the C-Mn structural steel specimens tested by Bertini [27] were subjected to PWHT may have had an impact on the FCG behaviour of the material by relaxing possible tensile (i.e. damaging) residual stresses in those specimens.

The comparison of FCG trends from a wide range of steels in Fig. 6 demonstrates that some variation can be observed in the FCG behaviour of different steels tested under various loading conditions and on different specimen geometries. It can be observed in this figure that for a given value of ΔK the FCG rate for various materials considered in this study varies by a factor of approximately three above and below the trend obtained from the tests on S355 G10 + M HAZ specimens. Also included in Fig. 6 are the proposed trends for welded joints from BS7910 based on the simplified law and 2-stage law. The comparison in
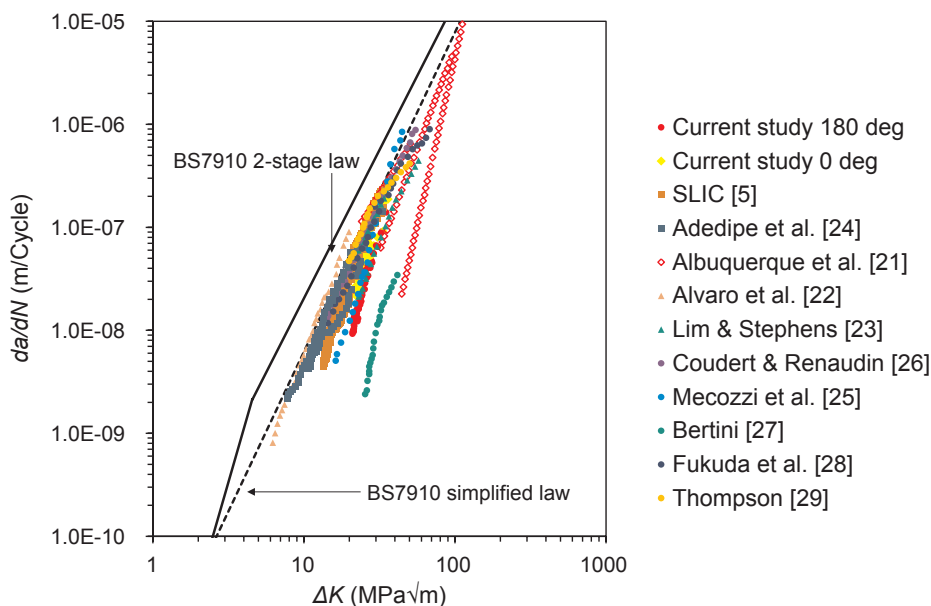

Fig. 6. Fatigue crack growth data on HAZ material in air compared with the literature data and BS7910 curves.

this figure shows that for the range of materials considered, the majority of data points fall upon or below the simplified law proposed by BS7910. These results show that although BS7910 2-stage law provides a conservative prediction of the FCG behaviour for the materials considered in this study, the recommended trend is not overly conservative and the upper bound fatigue data points fall only slightly below the 2-stage BS7910 curve. The Paris law constant for each of the HAZ materials considered in this study, and presented in Fig. 6, are summarised in Table 3. It can be seen in Fig. 6 and Table 3 that although the Paris law coefficient, C, and Paris law constant, m, show some variation for the range of materials considered in this study, the average slope from the experimental data is similar to the simplified law proposed in BS7910.

5. Residual stress measurements

In this study, residual stresses in three of the extracted C(T) samples (HAZ 2, HAZ 3 and HAZ 4) were measured non-destructively along three principal directions using the neutron diffraction technique. The direction of interest presented in this work corresponds to the transverse residual stresses, which are perpendicular to the direction of crack propagation and parallel to the loading direction in fracture mechanics tests on C(T) specimens. Measurements were performed on C(T) specimens post-machining and prior to pre-fatigue cracking.

5.1. Neutron diffraction test set-up on Engin-X

Neutron diffraction measurements were performed on the Engin-X instrument at the Rutherford Appleton Laboratory spallation source in Didcot, UK, where the neutron speed is measured by timing their passage over a known distance while the angle of scattering is fixed [30]. In these measurements, the lattice deformation is measured following Bragg's law [31]:

$$n\lambda = 2d_{hkl}\sin\theta \tag{3}$$

where n is a constant, λ is the wavelength of the characteristic rays, hkl are the Miller indices defining the lattice planes, d_{hkl} is the lattice interplanar spacing and θ is the incidence angle (Bragg's angle).

Subsequently, the residual strains can be calculated using the following equation:

$$\varepsilon_{hkl} = \frac{d_{hkl} - d_{0,hkl}}{d_{0,hkl}} \tag{4}$$

where ε_{hkl} is the residual strain corresponding to the hkl plane, d_{hkl} is the lattice interplanar spacing of the crystal measured and $d_{0,hkl}$ is the lattice interplanar spacing of the strain-free sample.

The errors in the strain measurements are also calculated as follows:

$$\varepsilon_{err} = \sqrt{\frac{d_{err}^2}{d^2} + \frac{d_{0,err}^2}{d_0^2}} \tag{5}$$

where ε_{err} is the error in the strain measurements, d_{err} is the error in the d-spacing measurements and $d_{0,err}$ is the error in the d-spacing measurements of the strain-free sample.

Consequently, the residual stresses can be calculated using the equation below [32].

$$\sigma_i = \frac{E_{hkl}}{1 + \nu_{hkl}}\varepsilon_i + \frac{\nu_{hkl}E_{hkl}}{(1 + \nu_{hkl})(1 - 2\nu_{hkl})}(\varepsilon_1 + \varepsilon_2 + \varepsilon_3) \tag{6}$$

where σ_i is the residual stress corresponding to ε_i residual strain, E_{hkl} is the Young's modulus of the hkl plane, ν_{hkl} is the Poisson's ratio of the hkl plane and ε_1, ε_2, ε_3 are the residual strains in the first, second and third directions respectively.

The error in the residual stress is calculated as per the following equation:

$$\sigma_{erri} = \sqrt{\left(\frac{E_{hkl}}{1 + \nu_{hkl}}\varepsilon_{erri}\right)^2 + \left(\frac{\nu_{hkl}E_{hkl}}{(1 + \nu_{hkl})(1 - 2\nu_{hkl})}\right)^2 \times (\varepsilon_{err1}^2 + \varepsilon_{err2}^2 + \varepsilon_{err3}^2)} \tag{7}$$

where σ_{erri} is the error in the residual stress measurements, corresponding to the error in the residual strain measurements ε_{err} and ε_{err1}, ε_{err2}, ε_{err3} are the errors in the strain measurements in the first, second and third directions respectively. Note that the analysis has been performed employing the elastic bulk properties of $E = 196$ GPa and $\nu = 0.3$ in the analysis [33].

Residual stress measurements were performed using a gauge volume of $2 \times 2 \times 2$ mm^3 at the mid-thickness and mid-height of the sample, along the crack propagation direction (i.e. specimen symmetry line). Moreover, d_0 measurements have been performed on 10 small cubes of $3 \times 3 \times 3$ mm^3 extracted from the exact same region of the crack path in the main C(T) specimen using the EDM technique. Further details on the neutron diffraction test set-up can be found in [9].

5.2. Neutron diffraction results

The residual stress measurements in a transverse direction, at mid-height and mid-thickness, from HAZ 2, HAZ 3 and HAZ 4 are presented against the distance from the crack tip in Fig. 7. It can be seen in Fig. 7 that in the examined HAZ specimens the RS values at the crack tip are around $+100$ MPa and -100 MPa while the peak stresses are between $+400$ MPa and -400 MPa. It is evident from Fig. 7 that there is high level of compressive residual stresses on HAZ 3 and HAZ 4 while on HAZ 2 a combination of tensile and compressive residual stresses can be observed. Such levels of transverse residual stresses are expected to influence the FCG behaviour of the material, particularly at the early stages of the test.

6. Numerical analysis of residual stress effects on fatigue crack growth using ΔK_{eff} parameter

In order to accurately characterise the effect of residual stresses on the FCG behaviour of HAZ samples with measured residual stress profiles, finite element analyses (FEA) have been performed to numerically calculate the effective SIF ΔK_{eff} at different stages of the tests. Such studies have previously been performed by Bao et al. [34] using the ANSYS software package and, based on the superposition rule of LEFM, the total SIF has been calculated. Bozic et al. also studied FCG in a welded stiffened panel specimen by using power law models, taking into account the effect of residual stresses by introducing the effective SIF ratio [35,36].

Table 3
Simplified Paris law constants for da/dN in m/Cycle and ΔK in MPa√m for the HAZ.

| Material	C	m
S355 G10 + M 180°	1.85×10^{-15}	5.10
S355 G10 + M 0°	1.58×10^{-13}	3.96
S355 G8 + M [5]	8.63×10^{-14}	4.26
S355 NL [21]	1.15×10^{-12}	3.19
420 MPa structural steel [22]	6.76×10^{-13}	3.94
4140 vacuum-degassed high tensile steel [23]	3.68×10^{-12}	2.95
S355 J2 + N [24]	5.66×10^{-12}	2.88
S355 EMZ high strength steel [25]	3.16×10^{-15}	5.10
SE702 steel [26]	3.15×10^{-12}	3.14
C-Mn structural steel [27]	5.19×10^{-17}	5.54
C-Mn-V steel [28]	3.55×10^{-12}	3.04
50D steel [29]	5.04×10^{-11}	2.35
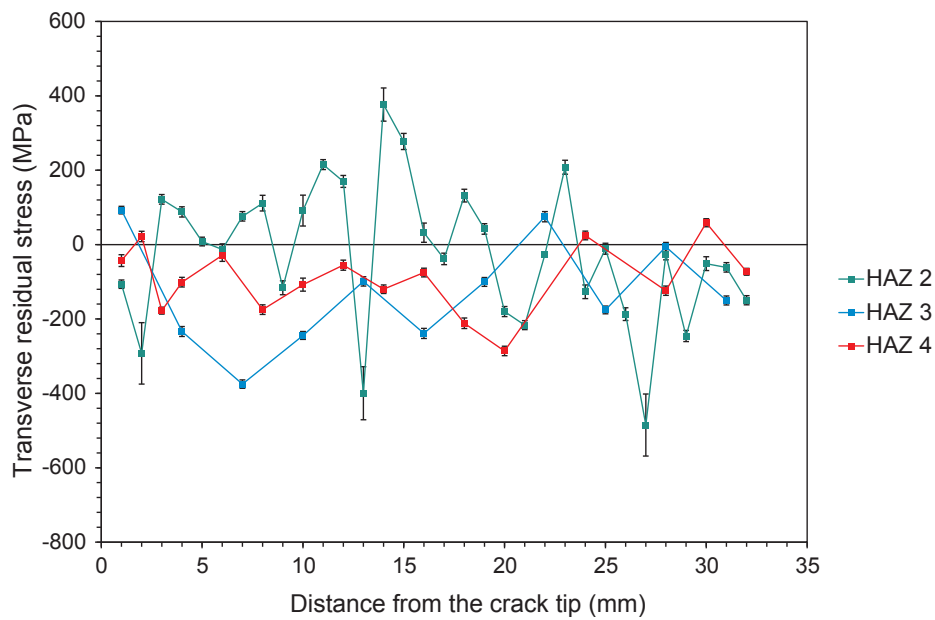
Fig. 7. . Transverse residual stresses on HAZ 2, HAZ 3 and HAZ 4 along the crack direction and before pre-cracking.

6.1. Finite element model set-up

ABAQUS CAE was employed to design the 2D model and to perform the FEA simulations. Only half of the specimen was designed by applying the Y-symmetry boundary condition (BC) to the crack line, in order to minimise the total number of elements and, therefore, the computational time. The material, with the elastic properties summarised in Table 4, was defined and assigned to the proper section representing the specimen.

Moreover, another material was specified with a Young's modulus of 100,000 GPa and the same Poisson's ratio. This extremely rigid material was assigned to the section corresponding to the pin hole in order to avoid possible deformations due to the application of the load on this section. Plane strain conditions were applied to the 2D model as the specimen is a thick component with a real thickness of 16 mm. The first model created for the introduction of residual stresses only used BCs and no external load was applied. A finer mesh was considered along the crack line in order to obtain more accurate results, as seen in Fig. 8. The mesh consists of 4-node bilinear elements with reduced integration. Each small rectangle corresponds to 1 mm over which the mesh seeds were divided every 0.25 mm.

For the purpose of model validation, a mesh sensitivity analysis was performed in order to individuate the optimal mesh to achieve reliable results. The details of the mesh sensitivity analysis are not presented in this paper for brevity, though the optimum element size along the crack path was found to be 0.25 mm.

6.2. Introduction of residual stress profile in the FEA model

The RS profile introduced in the FEA model is based on the residual stress measurements previously presented in Fig. 7 from the neutron diffraction tests. Three models have been created for the three different HAZ samples considered, with known RS profiles (i.e. HAZ 2, HAZ 3 and HAZ 4). As ABAQUS automatically applies a force balance after
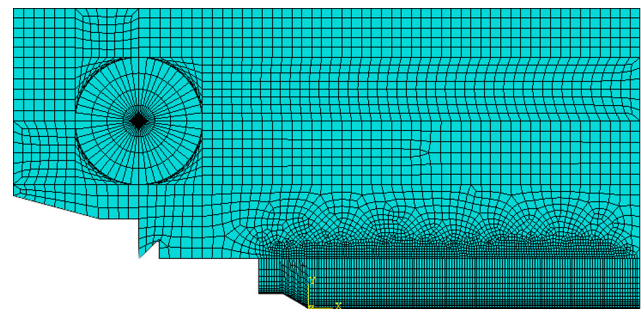

Fig. 8. Mesh design for the C(T) specimen symmetric model.

defining the initial BCs, the first step in the numerical analysis was to find the correct RS input values to introduce in the FEA model. To do so, an iterative process was implemented using a Python code and the user subroutine SIGINI, which is used to define all active initial stress components at material points. A diagram of the numerical iterative process is presented in Fig. 9, where k is the iteration number.

The general purpose of this procedure is to define an initial stress field at known distances from the crack tip where residual stresses were previously measured using neutron diffraction tests. The results at the end of the iterations are presented in Fig. 10 for HAZ 2, HAZ 3 and HAZ 4, with the RS target corresponding to the RS measured from neutron diffraction.

It can be seen in Fig. 10 that for HAZ 2 more data points were considered for the iteration process since finer neutron diffraction residual stress measurements were performed on this sample. A linear interpolation between the available data points was applied in all simulations where the target RS value at a given node was not available from the neutron diffraction measurements. It was found that the error between the target and the iteration curves are minor, as can be seen from the results on HAZ 3 and HAZ 4, where fewer data points from the

Table 4
Specimen dimensions, properties and fatigue test parameters.

Environment	W (mm)	B (mm)	a_0 (mm)	a_f (mm)	f (Hz)	R	P_{max} (kN)	ν	E (GPa)
Air	50	16	17	35	5	0.1	10	0.3	196

Step 1 — Definition $\sigma_{RS,target}$

Step 2 — Introduction of σ_{in} using SIGINI

Step 3 — Automatic ABAQUS force balance

Step 4 — $\sigma_{out,k} \approx \sigma_{RS,target\ k}$ $k = 0 \to 124$ — Yes → Iteration completed

No

Step 5 — $\sigma_{in}^{i+1} = \sigma_{in}^{i} + \beta(\sigma_{RS,target} - \sigma_{out}^{i})$ New SIGINI file
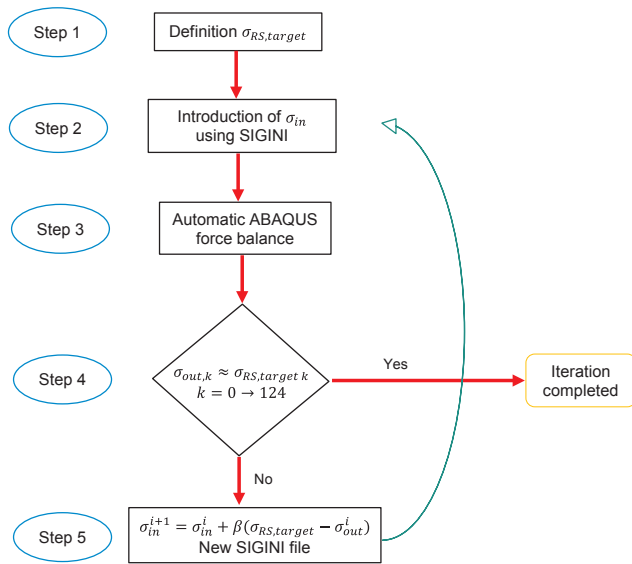
Fig. 9. Diagram of the iterative procedure for RS introduction.

neutron diffraction measurements were available due to coarser neutron diffraction measurements.

An example of the RS redistribution after the force balance achieved by iterations on HAZ 2 can be seen in Fig. 11. Although the stress components were introduced only into the crack line, the software ABAQUS redistributes the RS within the whole specimen during the simulation. Bearing in mind that this stress distribution should be mirrored with respect to the symmetry axis, the RS distribution influences the elements along the whole crack line.

6.3. Fatigue test simulation in the presence of residual stresses

Once the target RS values are obtained by iterating the input values in the SIGINI file, the FEA model accurately represents the real specimen condition by taking into consideration the initial RS profile. The next phase consists of replicating, using ABAQUS, the real test executed in the laboratory on the HAZ samples. The first significant modification of the FEA model is to simulate the crack propagation. In ABAQUS, it is
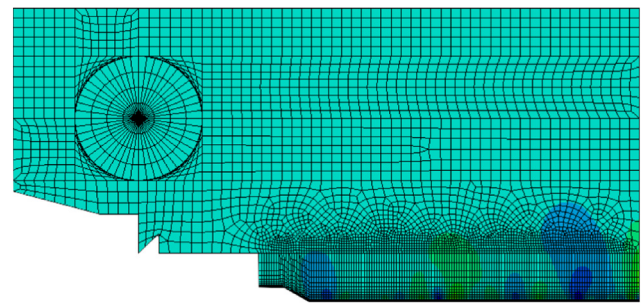

Fig. 11. RS distribution at the end of the iteration process on HAZ 2.

possible to create a crack initiation, selecting manually the crack front and specifying the direction of the crack extension; however, this process is valid only for quasi-static cracks. Since the purpose of this work is to reproduce a fatigue test condition, a dynamic crack propagation approach was necessary; however, it was found unnecessary to simulate crack propagation for examination of the RS effects on the FCG trend as a part of this study. Subsequently, according to the ASTM standard [14], which states that the fatigue test needs at least 18 mm of crack propagation, a further 18 steps were created. The aim at this step was to represent the crack propagation by debonding the nodes from the BCs (Y-symmetry) at every 1 mm at each step. Therefore, at every step the nodes are released, hence the crack advances by 1 mm, until the last 18th millimetre. An example of the procedure is shown in Fig. 12.

The second modification concerns the application of external loads. As summarised in Table 4 in the previous section, the fatigue test was performed with an R ratio of 0.1, a maximum load P_{max} of 10 kN and consequently a minimum load P_{min} of 1 kN. In ABAQUS, these factors are represented with two different FEA models, both derived from the FEA model used for the iteration with the first adjustment made. For both models, a load was created as a concentrated tensile force and was applied to the centre of the pin hole along the direction perpendicular to the crack plane with a magnitude of 10,000 N for the P_{max} model and 1,000 N for the P_{min} one. Both loads were set up with a tabular amplitude required to simulate the periodical and sinusoidal fatigue tests. The results from both simulations are needed in order to obtain reliable outcomes to compare with the experimental data, and to calculate maximum and minimum SIFs in the presence of residual stresses, $K_{max,RS}$ and $K_{min,RS}$, and subsequently calculate the effective SIF range,
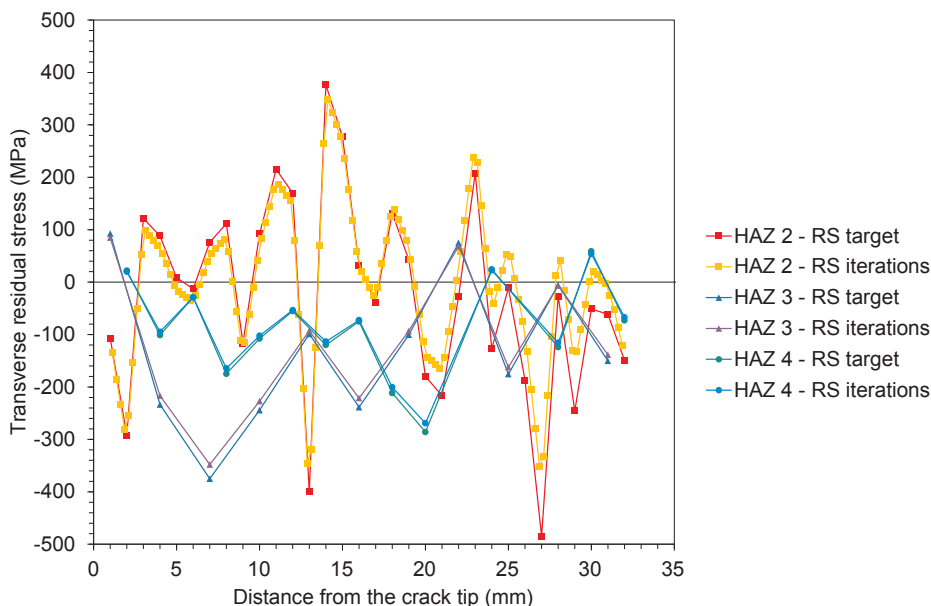

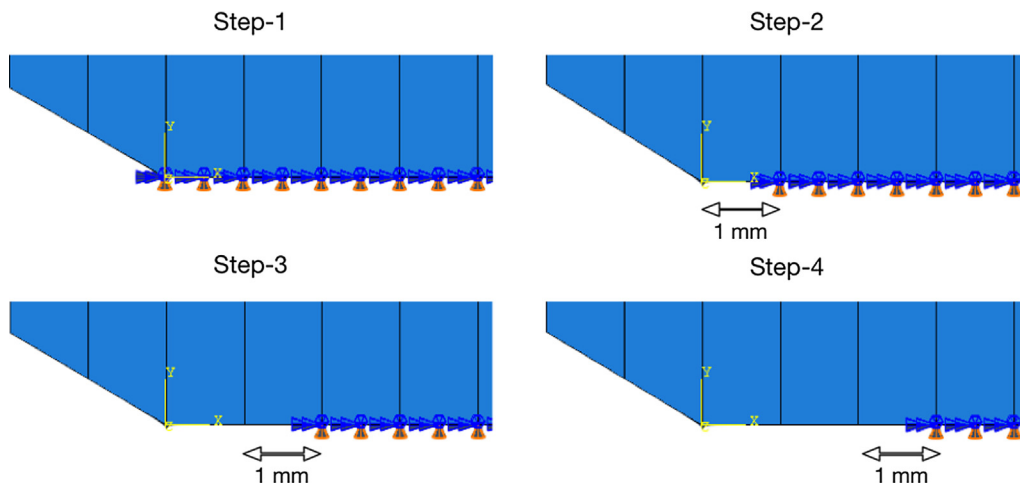**Fig. 10.** RS target and RS at the end of the iteration process on the three HAZ considered.

Fig. 12. Example of crack propagation unbinding nodes from Boundary Conditions (BCs) every 1 mm.

ΔK_{eff}, in the presence of residual stresses. Both models were run with these modifications after introducing the initial residual stress profile in the model.

The loading effect in the presence of RS has been shown for HAZ 4 in Fig. 13 as an example. The state of RS can be seen in this figure, at the end of the iterations, under 1 kN and under 10 kN. The residual stress profile has been found to slightly and more severely shift up by applying the minimum and maximum applied load, respectively. It can be seen in Fig. 13 that under small loading conditions, the state of RS before any crack growth is very similar to the one without any external load applied. Moreover, under 10 kN, the state of RS is higher, especially near the crack tip. These observations demonstrate numerically the loading effect in the presence of RS using ABAQUS.

6.4. Stress intensity factor calculation

Several methods exist to calculate the SIF from ABAQUS simulations following a direct or indirect approach. One of the indirect methods is the Virtual Crack Closure Technique (VCCT) which was chosen for the SIF computation in this work. This approach is well known in the literature [37], especially to calculate the SIF through FEA simulations

[38–40]. The VCCT is an indirect method to calculate the SIF from FE simulations. It is based on Irwin's energy principle [41], and relates to the SIF and strain energy release rate, G, following the equation below:

$$G = \frac{K^2}{E}(1 - \nu^2) \quad plane \;\; strain \tag{8}$$

where K is the SIF, E is the Young's modulus and ν is the Poisson's ratio of the material.

The strain energy release rate G is the amount of energy dissipated per unit crack growth per unit thickness. Since it depends on the thickness, the equation varies according to the plane stress or plane strain conditions. The VCCT relies on the estimation of G, considering the nodal vertical displacement of the nodes involved in the crack propagation and the nodal reaction force of the new crack tip for a defined crack advance and for a fixed thickness. The parameters involved are shown in Fig. 14.

For a crack propagation Δa, the nodal vertical displacements of the two nodes involved in the crack opening, are taken into consideration. The nodal reaction force is evaluated from the new crack tip after the crack advance. All these parameters can be extracted from an ABAQUS simulation post-processing the outcomes. The strain energy release rate is then calculated using the following equation.
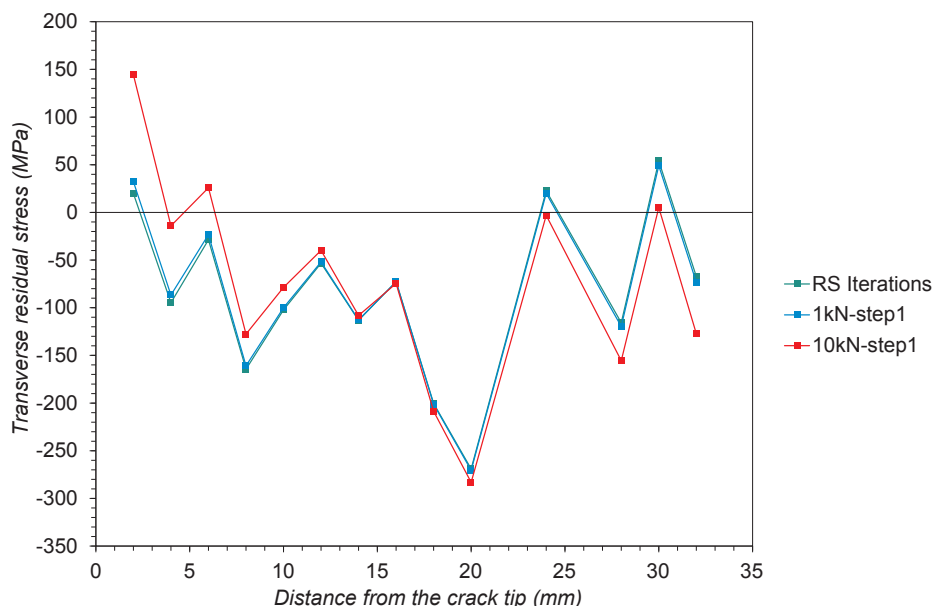

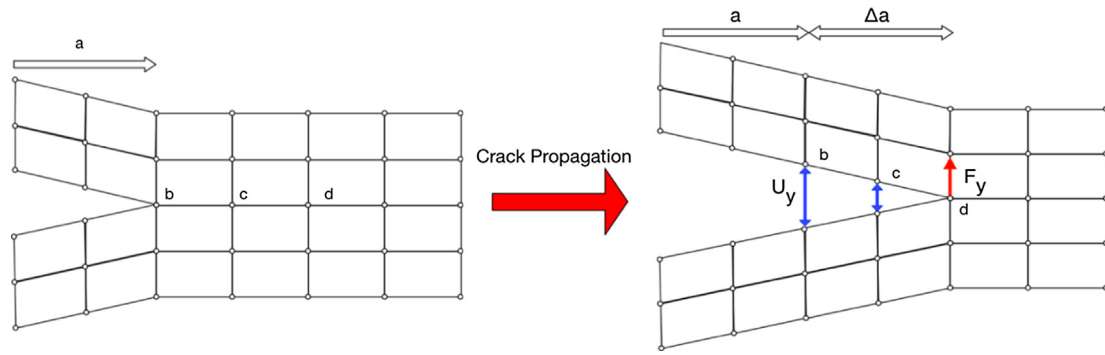**Fig. 13.** Residual stress state at the end of the iterations and under loading on HAZ 4.

Fig. 14. Parameters involved in the VCCT to calculate *G* from ABAQUS results.

$$G = -\frac{1}{2t\Delta a}[F_{y,d}U_{y,b} + F_{y,d}U_{y,c}] \tag{9}$$

The calculation of G, and consequently K, was performed at each step of the FCG simulation. The thickness of 16 mm has been considered due to the plane strain conditions. This procedure has been performed at each step in order to obtain different K values as a function of the distance from the crack tip, for both models under P_{max} and P_{min} respectively. The SIF range ΔK_{eff} is then calculated at every step following the equation below.

$$\Delta K_{eff} = K_{max,RS} - K_{min,RS} \tag{10}$$

where $K_{max,RS}$ is the SIF calculated from the model under P_{max} of 10 kN in the presence of RS and $K_{min,RS}$ is the one from the model under P_{min} of 1 kN. In order to confirm the results obtained, the accuracy of the VCCT technique has been verified by comparing the results with the contour integral method performed by ABAQUS and it has been shown that

after a few contours the SIF values tend to converge.

Finally, it is worth noting that the redistribution of the RS during crack growth is unachievable by ABAQUS. Indeed, the process employed here is similar to the weight function approach [42] where the initial residual stress profile is taken into consideration without accounting for subsequent RS redistribution. Prediction and validation of residual stress redistribution is beyond the scope of this study and is a subject for further investigation in the future.

6.5. Residual stress effects on near threshold fatigue crack growth behaviour

The results from the calculations previously described are compared with the experimental data for HAZ 2, HAZ 3 and HAZ 4 and start from a 4 mm pre-crack to avoid taking into account the pre-fatigue cracking data. In the following figures, ΔK_{eff} is the effective SIF range calculated from the numerical analysis accounting for the RS and ΔK_{app} is the
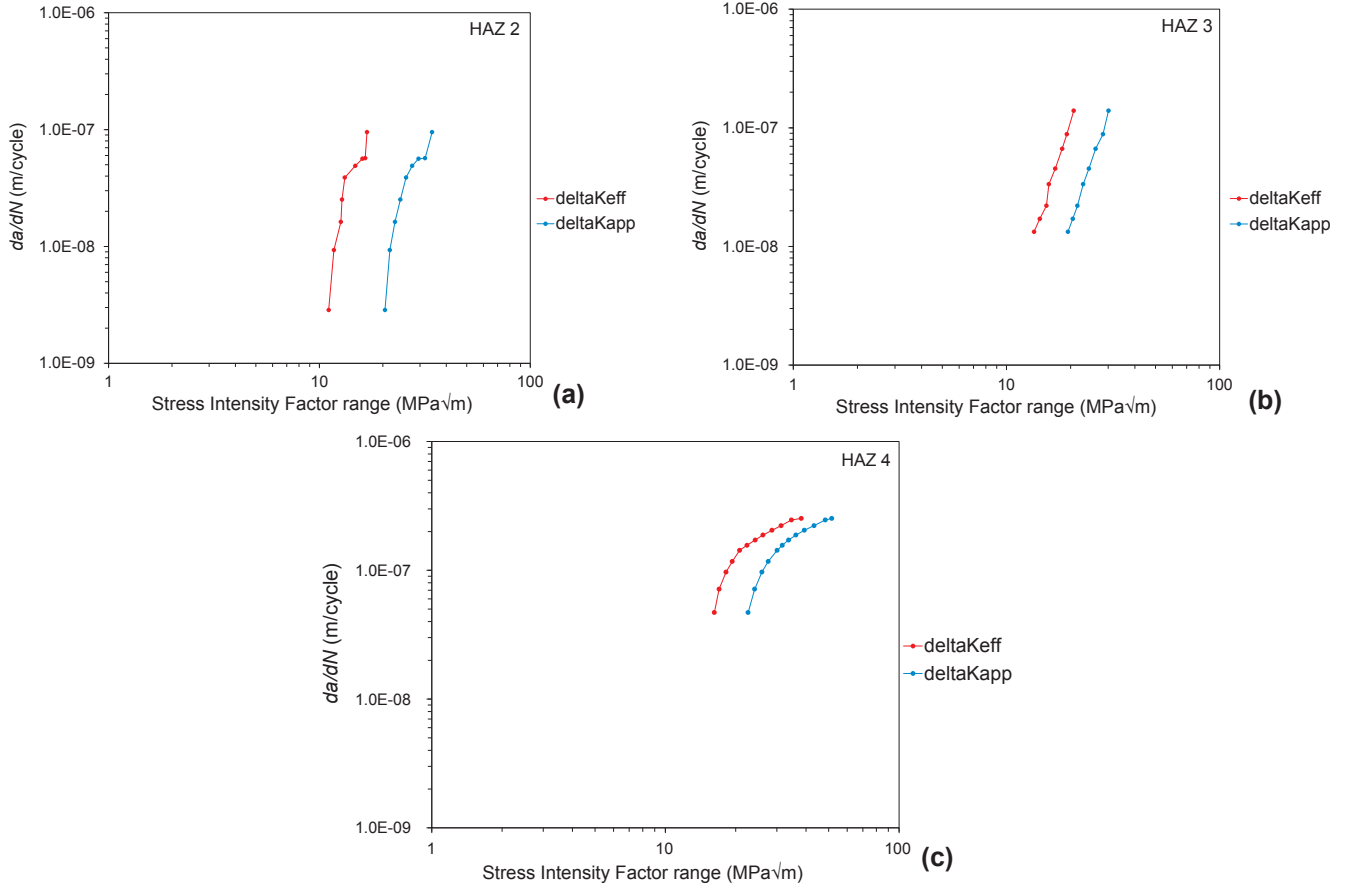

Fig. 15. Numerical and experimental FCG behaviour of (a) HAZ 2, (b) HAZ 3 and (c) HAZ 4.

experimental (i.e. applied) SIF range taking into account only the global load applied during the actual experiments.

It is important to note that the da/dN values for both curves represented in each graph have been taken from the experimental data available for the corresponding crack growth. It can be seen in Fig. 15 that the presence of RS tends to influence the FCG behaviour of the material in the air environment. In all three cases, the effective FCG behaviour presented lower SIF range values in the near threshold region for a given value of da/dN. This effect has been observed in [41,43]. It would also be expected to see the curve from ΔK_{eff} overlap with the curve from ΔK_{app} in the Paris region, as the RSs tend to redistribute to finally vanish as the crack propagates [16,17]. The shift in effective SIF in HAZ 3 and HAZ 4, where the RSs were predominantly compressive, is less than 10 $MPa\sqrt{m}$ and similar in both samples. Finally, a greater shift in the effective SIF is observed in HAZ 2, in which neutron diffraction measurements have shown a larger level of fluctuation in RS values along the crack propagation direction.

As a future work, it is suggested to compare analytically calculated SIF values with FEA results, considering the applied load only, without RSs. This would help to calibrate the FEA model for the subsequent calculation of SIF values taking into account RSs. Moreover, corrosion-fatigue crack growth tests will be conducted in future work to examine the combined effects of RS and corrosion damage on the FCG behaviour of the material.

7. Conclusions

A combined experimental-numerical study has been performed in this work to examine the influence of welding residual stresses on fatigue crack growth behaviour of S355 structural steel, which is widely used in the fabrication of offshore wind turbine monopile foundations. The experimental results from fatigue crack growth tests in air have shown that the specimen orientation, with respect to the weld geometry, plays a significant role in fatigue crack growth behaviour of the material and for a given value of ΔK the specimens with 0° orientation show on average around twice higher fatigue crack growth rates compared to the specimens with 180° orientation. Neutron diffraction measurements have been performed on three of the extracted HAZ specimens, selected from two different specimen orientations, and the results have shown residual stress values of around +100 MPa and −100 MPa at the crack tip with peak residual stress values of between +400 MPa and −400 MPa along the transverse direction. In order to examine the influence of residual stresses on near threshold fatigue crack growth behaviour of the material, a numerical model has been built up in ABAQUS where residual stresses are introduced into the model through an iterative process using the SIGINI subroutine and a Python code. The numerical results obtained from the characterised HAZ specimens with measured residual stress profiles have shown that for a given value of da/dN the effective stress intensity factor range in the near threshold region is up to 10 MPa√m lower compared to the applied stress intensity factor range. The shift of the analysed fatigue crack growth trend in the presence of residual stresses to lower values of ΔK is thought to be due to dominantly compressive residual stress profiles in the HAZ specimens examined using numerical simulations. Finally, it is expected that the curve from ΔK_{eff} overlaps with the curve from ΔK_{app} in the Paris region, if the redistribution of the residual stresses was to be modelled in numerical simulations.

Acknowledgements

Appendix A. Supplementary material

Supplementary data to this article can be found online at https://doi.org/10.1016/j.ijfatigue.2019.105196.

References

[1] Owusu PA, Asumadu-Sarkodie S. A review of renewable energy sources, sustainability issues and climate change mitigation. Cicil Environ Eng 2016;3.
[2] Jensen PH, Chaviaropolos T, Natarajan A. LCOE reduction for the next generation offshore wind turbines; 2017.
[3] Smart G. Offshore Wind cost reduction recent and future trends in the UK and Europe; 2016.
[4] Energy UK. Offshore wind market development and cost reduction background; 2018.
[5] Mehmanparast A, Brennan F, Tavares I. Fatigue crack growth rates for offshore wind monopile weldments in air and seawater: SLIC inter-laboratory test results. Mater. Des. 2017;114:494–504.
[6] Manwell JF, McGowan JG, Rogers AL. Wind energy explained: theory, design and application. John Wiley & Sons; 2010.
[7] Scharff R, Siems M. Monopile foundations for offshore wind turbines–solutions for greater water depths. Steel Construct 2013;6(1):47–53.
[8] Musial W, Butterfield S, Ram B. Energy from offshore wind. In: Offshore technology conference; 2006. 1–11.
[9] Jacob A, Oliveira J, Mehmanparast A, Hosseinzadeh F, Kelleher J, Berto F. Residual stress measurements in offshore wind monopile weldments using neutron diffraction technique and contour method. Theoret Appl Fract Mech 2018;96:418–27.
[10] Veritas, Det Norske. Offshore Standard DNV-OS-B101 Metallic Materials; 2009.
[11] Peeringa J, Bedon G. Fully integrated load analysis included in the structural reliability assessment of a monopile supported offshore wind turbine. Energy Procedia 2017;137:255–60.
[12] Velarde J, Bachynski EE. Design and fatigue analysis of monopile foundations to support the DTU 10 MW offshore wind turbine. Energy Procedia 2017;137:3–13.
[13] Norske, Veritas Det. Fatigue design of offshore steel structures; 2005.
[14] ASTM International. Standard test method for measurement of fatigue crack growth rates; 2010.
[15] British Standard Institution. BS ISO 12108:2012, Metallic materials - Fatigue testing - Fatigue crack growth method, London; 2012.
[16] Lam YC, Lian KS. The effect of residual stresses and its redistribution on fatigue crack growth. Theor Appl Fract Mech 1989;12:59–66.
[17] James MR. The relaxation of residual stresses during fatigue. In: Residual stress and stress relaxation; 1982. p. 297–8.
[18] The British Standards Institution. BSI standards publication guide to methods for assessing the acceptability of flaws in metallic structures; 2015.
[19] Park H-B, Lee B-W. Effect of specimen thickness on fatigue crack growth rate. Nucl Eng Des 2000;197(1–2):197–203.
[20] Costa JDM, Ferreira JAM. Effect of stress ratio and specimen thickness on fatigue crack growth of CK45 steel. Theor Appl Fract Mech 1998;30(1):65–73.
[21] Albuquerque CMC, Miranda RMC, Richter-Trummer V, de Figueiredo MAV, Calçada R, de Castro PMST. Fatigue crack propagation behaviour in thick steel weldments. Int J Struct Integr 2012;3(2):184–203.
[22] Alvaro A, Akselsen OM, Ren X, Kane A. Fatigue properties of a 420 MPa structural steel at low temperature. In: Proceedings of the twenty-sixth international ocean and polar engineering conference; 2016. p. 331–7.
[23] Stephens RI, Lim JK. Fatigue crack growth and retardation in the welded HAZ of 4140 steel. Weld Res Suppl 1990:294–304.
[24] Adedipe O, Brennan F, Mehmanparast A, Kolios A, Tavares I. Corrosion fatigue crack growth mechanisms in offshore monopile steel weldments. Fatigue Fract Eng Mater Struct 2017;40(11):1868–81.
[25] Mecozzi E, Lecca M, Sorrentino S, Large M, Davies C, Gouveia H, et al. Fatigue behaviour of high-strength steel-welded joints in offshore and marine systems (FATHOMS). Mecozzi, M. Lecca, S. Sorrentino-Office for Official Publ. of the European Communities; 2010. p. 179.
[26] Coudert E, Renaudin C. Variable amplitude corrosion fatigue behaviour and hydrogen embrittlement of high strength steels for offshore applications. Int Offshore Polar Eng Conf 1998;IV:116–22.
[27] Bertini L. Influence of seawater and residual stresses on fatigue crack growth in C - M n steel weld joints. Theor Appl Fract Mech 1991;16:135–44.
[28] Fukuda T, Iwadate T, Shimazaki M. "Consideration on the scatter of COD and fatigue crack propagation characteristics of heavy section C-Mn-V forged steel for offshore structure. Offshore Technol Conf 1982:109–12.
[29] Thompson JWC. Phenomenological investigation of the influence of cathodic protection on corrosion fatigue crack propagation behaviour, in a BS 4360 50D type structural steel and associated weldment micro-structures, in a marine environment; 1984.
[30] International Atomic Energy Agency (IAEA). Measurement of residual stress in materials using neutrons. In: Proceedings of a technical meeting; 2003.
[31] Pynn R. Neutron scattering - a non-destructive microscope for seeing inside matter. Neutron scattering applications and techniques. Springer; 2009.
[32] Mehmanparast A, Davies CM, Nikbin KM. Quantification and prediction of residual stresses in creep crack growth specimens. Mater Sci Forum 2014;777:25–30.
[33] Hutchings MT, Withers PJ, Holden TM, Lorentzen T. Introduction to the characterization of residual stress by neutron diffraction. CRC Press; 2005.
[34] Bao R, Zhang X, Yahaya NA. Evaluating stress intensity factors due to weld residual

stresses by the weight function and finite element methods. Eng Fract Mech 2010;77(13):2550–66.

[35] Božić Ž, Schmauder S, Wolf H. The effect of residual stresses on fatigue crack propagation in welded stiffened panels. Eng Fail Anal 2018;84:346–57.

[36] Božić Ž, Schmauder S, Mlikota M, Hummel M. Multiscale fatigue crack growth modelling for welded stiffened panels. Fatigue Fract Eng Mater Struct 2014;37(9):1043–54.

[37] Krueger R. Virtual crack closure technique: history, approach, and applications. Appl Mech Rev 2004;57(2):109–43.

[38] Leski A. Implementation of the virtual crack closure technique in engineering FE calculations. Finite Elem Anal Des 2007;43(3):261–8.

[39] Rybicki EF, Kanninen MF. A finite element calculation of stress intensity factors by a modified crack closure integral. Eng Fract Mech 1977;9(4):931–8.

[40] Busse D. Extending fatigue life of aircraft fuselage structures using laser-peening. Cranfield University; 2017.

[41] Schijve J. Fatigue of Structures and Materials 2009.

[42] Zhao W, Wu XR, Yan MG. Weight function method for three dimensional crack problems—II. Application to surface cracks at a hole in finite thickness plates under stress gradients. Eng Fract Mech Jan. 1989;34(3):609–24.

[43] Elber W. The significance of fatigue crack closure. In: Rosenfeld M, editor. Damage tolerance in aircraft structures. West Conshohocken, PA: ASTM International; 1971. p. 230–42.